Surface and subsurface phonons of Bi(111) measured with helium atom scattering

Anton Tamtögl,[1,*] Patrick Kraus,[1] Michael Mayrhofer-Reinhartshuber,[1] Davide Campi,[2] Marco Bernasconi,[2] Giorgio Benedek,[2,3] and Wolfgang E. Ernst[1]

[1]*Institute of Experimental Physics, Graz University of Technology, Graz, Austria*

[2]*Dipartimento di Scienza dei Materiali, Università degli Studi di Milano-Bicocca, Milano, Italy*

[3]*Donostia International Physics Center (DIPC), University of the Basque Country (EHU-UPV), Donostia, San Sebastian, Spain.*

(Received 22 October 2012; published 10 January 2013)

The surface phonon dispersion curves of Bi(111) have been measured by inelastic helium atom scattering (HAS) along the two symmetry directions. The complex set of observed dispersion curves, including several branches in the acoustic region, plus a localized and a resonant branch in the optical region, is interpreted by means of calculations based on density functional perturbation theory (DFPT). It is recognized that the upper phonon branches in the acoustic region starting at about 5.3 meV and 4.3 meV at zero wave vector correspond to shear-vertical and longitudinal modes localized on the third surface layer (second bilayer), respectively. The HAS ability of detecting subsurface phonons previously observed for Pb(111) multilayers is attributed to the comparatively strong electron-phonon interaction, and confirmed through a DFPT calculation of the phonon-induced surface charge-density oscillations. A comparison of the integrated HAS intensities with those of Pb(111) multilayers measured under similar kinematic conditions allows for an estimation of the electron-phonon mass-enhancement parameter for the Bi(111) surface. An anomaly at the $\overline{\mathrm{M}}$ point, quite sharp at 123 K but very broad at room temperature, is associated with recombination processes of bulk $\overline{\mathrm{M}}$-point pocket electrons with bulk pocket holes at either $\overline{\Gamma}$ or equivalent $\overline{\mathrm{M}}$ points.

DOI: 10.1103/PhysRevB.87.035410 PACS number(s): 63.22.−m, 68.49.Bc, 34.50.−s, 34.35.+a

I. INTRODUCTION

The stable rhombohedral forms of Group-V (Bi, Sb, As) semimetals exhibit a layered structure formed by a stacking of (111)-oriented atomic bilayers with stronger intra-bilayer and weaker inter-bilayer bonds. An intriguing aspect of these materials is that despite the comparatively weak interlayer bonding, the electronic structure and the electron-phonon properties of the surface bilayer are rather different from those of the bulk. In bismuth the semimetallic character is determined by narrow electron and hole pockets at symmetry points of the Brillouin zone boundary.[1] The surface induces pairs of electronic bands, spin-split due to a comparatively large spin-orbit coupling (SOC), across the Fermi level with extended electron and hole pockets.

A surprising theoretical fact is that a single bilayer is stable but insulating: Thus the conduction properties and their enhancement at the surface, which acquires a metallic character, are actually induced by the addition of bilayers beneath the surface bilayer. This indicates that the interaction between adjacent bilayers is strong enough to produce relevant surface effects. One of these effects is superconductivity. While in the bulk rhombohedral phase, which is not superconducting, the electron-phonon strength expressed by the mass-enhancement parameter λ is indeed very small ($\lambda \approx 0.13$),[2] rhombohedral Bi nanocrystals[3] and bicrystals with suitably oriented crystallite interfaces[4] exhibit superconductivity with T_c up to 6 K and 21 K, respectively. These results suggest a large enhancement of the electron-phonon coupling at the surface of Bi, consistent with the ARPES data of the Bi(111) surface from Ast and Höchst,[5] who reported values of λ ranging from 0.6 to 2.3, depending on the choice of the effective Debye frequency. On the other hand, a fitting of the temperature and binding energy dependence of the linewidth[1,6,7] gives rise to a smaller value ($\lambda = 0.4$), which would suggest a major contribution from bulk phonons, similarly to what has been reported for Sb(111).[8,9] Therefore, an investigation of the surface phonon dispersion curves of Bi(111) and the identification of the phonon modes with the strongest coupling to electronic transitions around the Fermi level are particularly needed.

It has recently been shown that inelastic helium atom scattering (HAS) intensities convey direct information on the electron-phonon coupling strength of individual surface phonons in ultrathin metal films.[10] This has motivated the present HAS investigation of the surface phonon dispersion curves in Bi(111) and their theoretical analysis based on density-functional perturbation theory (DFPT). With respect to HAS studies of ordinary low-index metal surfaces, semimetal surfaces present several complications related to the fact that the surface is corrugated and conducting at the same time. Corrugation is necessary for the occurrence of inelastic bound-state resonances that can be exploited to amplify weak one-phonon processes, in particular in the optical region.[11,12] Yet this can also cause undesired multiphonon features.

On the other hand, on a conducting surface He atoms transmit energy and parallel momentum to phonons via electron-phonon interaction[11] and a nonnegligible fraction of the atom kinetic energy can be transferred to the surface electron gas via electron-hole (e-h) excitations. For ordinary metal surfaces the latter processes are rather diffuse and not expected to produce specific features in the HAS time-of-flight (TOF) spectra. However, on semimetals where electrons are restricted to narrow pockets in the parallel momentum space, single e-h excitations may also give rise to inelastic features in the TOF spectra, which can be particularly evident in spectral regions were one-phonon processes are not expected.

The e-p scattering processes involving electron inter- and intrapocket transitions at the Fermi level are expected to be concentrated around certain values of the parallel momentum, possibly yielding Kohn anomalies. Recent HAS experiments

on the (111) surface of the topological insulator Bi_2Se_3 have revealed a deep anomaly in a phonon branch which has been attributed to the coupling with Dirac-cone electronic transitions and has been used to infer the e-p coupling strength.[13,14] Deep anomalies similar to that of H:W(110)[15] are characterized by a large charge-density (electron-hole) oscillation and vanishing atomic displacements, which makes them suitable to HAS spectroscopy but hardly visible to other techniques.

Another virtue of HAS spectroscopy for metal surfaces is based on the fairly long range e-p interaction and can also provide information on the dispersion of subsurface phonon modes. Notably, these modes can even be localized several layers beneath the surface as in the case of ultrathin lead films.[10] In the following a similar situation is shown to occur also for Bi(111) where phonons localized on the second bilayer contribute substantially to inelastic HAS intensities via the e-p coupling of surface electrons.

A. The Bi(111) surface

Bismuth crystallizes in the rhombohedral A7 structure with two atoms per unit cell; the crystal consists of puckered bilayers of atoms perpendicular to the [111] direction [Figs. 1(a) and 1(c)], with the inter-bilayer distance (2.347 Å) considerably larger then the intra-bilayer distance (1.594 Å).[16] The lattice parameters at 140 K of the slab-adapted hexagonal unit cell, encompassing three bilayers, are $a = 4.538$ Å and $c = 11.823$ Å.[16] As inferred from the bulk phonon structure[17,18] and the (111) surface dynamics described below, the inter-bilayer bonding is weaker than the covalent bonding within each bilayer, which makes cleavage easy along the (111) planes between two bilayers.[1] The inter-bilayer bonding of bismuth and and its group-V rhombohedral is considerably stronger than a pure van der Waals (vdW) bonding since it actually originates from the overlap of the back bonds of the strong *p*-type intralayer bonds.

Mönig *et al.*[16] determined the detailed structural parameters of Bi(111) with LEED and *ab initio* calculations and reported that the first bilayer thickness (first interlayer distance d_{12}) is slightly expanded with respect to the bulk value by $\leqslant 1\%$. The same holds for the first inter-bilayer distance d_{23} which is almost 2% larger than in the bulk. The second bilayer spacing d_{34} is practically equal to the bulk value. *Ab initio* calculations[16] correctly predict an expansion of the first interlayer distances, though only in a qualitative agreement with the experimental data extrapolated to 0 K. However, similar calculations with and without SOC for an increasing number N (1 to 5) of bilayers[19] show quantum size effects with a contraction of d_{12} and an expansion of d_{23} which oscillate with N and slowly converge to semi-infinite crystal values.

Although the two hollow sites in the surface unit cell [Fig. 1(a)] are crystallographically inequivalent, previous low-energy HAS measurements on Bi(111)[20] indicated a perfect equivalence of the two sites in the surface profile derived from the diffraction intensities, as it would be for a single hexagonal layer. In other words, in the case of elastic scattering He atoms do not perceive any influence of the atomic layers beneath the surface which is an indication of the dominant contribution of electronic surface states to the He-surface potential. This fact is confirmed by an *ab initio* calculation as shown in Fig. 1(d): The surface charge density seen by a He atom impinging vertically

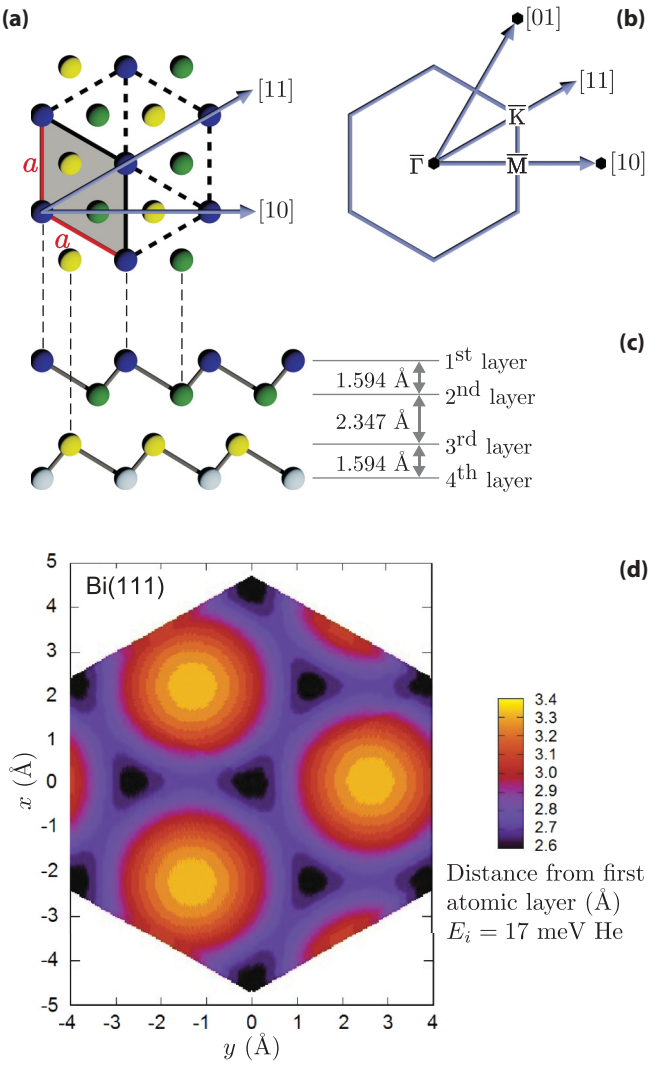

FIG. 1. (Color online) (a) Top view of the Bi(111) surface structure together with the two scattering directions. The rhombus (shadowed area) is the surface unit cell with $a = 4.538$ Å (interpolated to 140 K; Ref. 16); atoms of different color are on different planes, as illustrated in panel (c). Panel (b) shows the surface Brillouin zone with the symmetry points, the two reciprocal lattice basis vectors [10] and [01], and the scattering directions in the reciprocal space. The layered structure of Bi(111) is shown in (c) with the bulk interlayer distances at 140 K (Ref. 16); the slab-adapted hexagonal unit cell encompasses three bilayers ($c = 11.823$ Å). Although the two hollow positions in the surface unit cell (a) are crystallographically inequivalent, the calculated surface charge density (d) as seen by a He atom impinging vertically with an energy of 17 meV shows equivalent hollow sites as for a single hexagonal layer.

with an energy corresponding to the experiments (17 meV) exhibits indeed equivalent hollow sites. As illustrated in the following experiments, inelastic HAS is however sensitive to the motion of subsurface atomic layers, providing evidence of a long-range e-p interaction which couples surface electronic states to surface as well as bulk phonons.

II. EXPERIMENTAL DETAILS

All measurements of this work were performed on a HAS apparatus with a fixed 91.5° source-target-detector

geometry. A nearly monochromatic He beam ($\Delta E/E \approx 2\%$) was generated in a supersonic expansion of helium through a 10 μm nozzle and the central part of the beam was then selected using a 310 μm skimmer. The apparatus and its dimensions have been described elsewhere.[21]

The Bi(111) single crystal which has been used in this study was a disk with a diameter of 15 mm and a thickness of 2 mm. The crystal was mounted on the sample holder which is attached to a 6-axes manipulator and the sample temperature was measured using a chromel-alumel thermocouple. The crystal could either be heated resistively using a button heater or cooled down to 90 K using liquid nitrogen. Prior to the measurements the surface was cleaned by Ar^+ sputtering (1.5 kV, 2 μA) and annealing to 423 K. The good quality of the surface was approved by diffraction and the very small magnitude of the diffuse elastic peak.

Inelastic HAS spectra were measured with the time-of-flight (TOF) method at different incident angles θ_i and fixed incident energy $E_i = 17.7$ meV (incident wave vector $k_i = 1.08$ Å^{-1}, source temperature 82 K).[22] A pseudorandom chopper disk[23,24] with a sequence of 511 bits was used.[21] The TOF system was calibrated by comparing the incident energy from TOF measurements of the elastically scattered He atoms to that derived from the angular spacing of the diffraction peaks.

III. RESULTS

Figures 2 and 3 display a few exemplary TOF spectra converted to the energy-transfer (ΔE) scale for different incident angles and about the same incident energy along the directions $\overline{\Gamma K}$ (Fig. 2) and $\overline{\Gamma M}$ (Fig. 3), respectively. It is assumed that $\Delta E < 0$ (>0) corresponds to phonon creation (annihilation) processes. The scan curves (dot-dashed lines) are superimposed onto the spectra, providing for each value of ΔE the corresponding parallel momentum transfer (right-hand scale). The different symbols (squares, triangles, circles, lozenges) on the scan curves, marking the main inelastic features, have been associated with phonons of different character and polarization.

In order to identify the peak maxima and to resolve merged peaks, the spectra were least-squares fitted by multiple Gaussian peaks. The diffuse elastic peak at $\Delta E = 0$ (vertical dotted line in Figs. 2 and 3) is due to the small concentration of surface defects:[22] Its present comparatively low intensity is an indication of a high-quality surface.

To determine the entire phonon dispersion curve up to the Brillouin zone boundary a series of TOF spectra was measured at incident angles between the first-order diffraction peaks. The phonon dispersion was then obtained by transforming each TOF spectrum into an energy transfer spectrum from which the phonon energy $\Delta E = \hbar\omega$ was extracted. The parallel momentum transfer $|\Delta K|$ was calculated from the conservation laws of energy and parallel momentum providing the scan curve for planar scattering:[22,25,26]

$$\frac{\Delta E}{E_i} = -1 + \frac{\sin^2\theta_i}{\sin^2\theta_f}\left(1 + \frac{\Delta K}{K_i}\right)^2, \qquad (1)$$

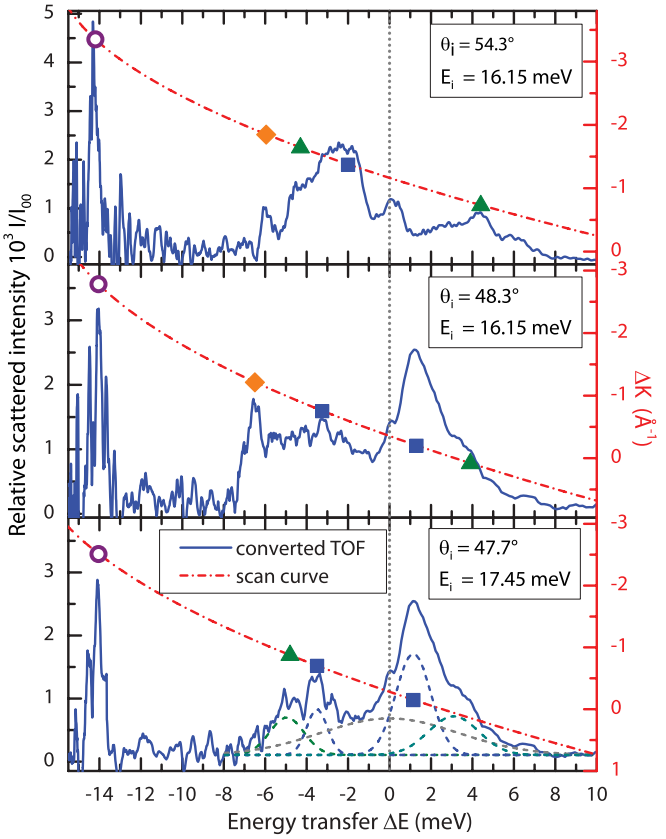

FIG. 2. (Color online) A few time-of-flight spectra converted to the energy transfer (ΔE) scale for different incident angles and about the same incident energy along the $\overline{\Gamma K}$ direction. $\Delta E < 0$ (> 0) corresponds to a phonon creation (annihilation) process. The scan curves (dot-dashed lines) allow reading the corresponding parallel momentum transfer on the right-hand scale. An example of a Gaussian fit of the spectrum on top of a multiphonon background is shown in the lowest panel (dashed curves). The symbols (squares, triangles, circles, lozenges) on the scan curves mark the main inelastic features and correspond to different phonon dispersion curves in Fig. 4. The crystal was cooled down to $T_S = 123$ K during the measurements.

where E_i is the energy of the incident beam, K_i is the parallel component of the incident wave vector, and θ_i and θ_f are the incident and final angle, respectively. The phonon parallel momentum is then given by $|\Delta K| + G$, where the surface reciprocal lattice vector G in the scattering plane, needed to bring Q into the first Brillouin zone, accounts for umklapp processes. A few hundred TOF spectra have been measured for both high-symmetry directions and for both a cooled sample (103 K along $\overline{\Gamma K}$ and 123 K in the $\overline{\Gamma M}$ direction) and a sample at room temperature (RT).

The phonon data points are plotted in Fig. 4. Their assignment to different phonon polarizations (represented by the different symbols) is based on a comparison with calculations; i.e., if an experimental data point falls close to a calculated dispersion curve it is likely to belong to this mode. Despite the appreciable spread of data points due to the limited resolution, a set of 4 or 5 dispersion curves in the acoustic region and two in the optical region is clearly distinguished. Considering that shear-horizontal (SH) phonon modes are not detected for symmetry reasons, the number of

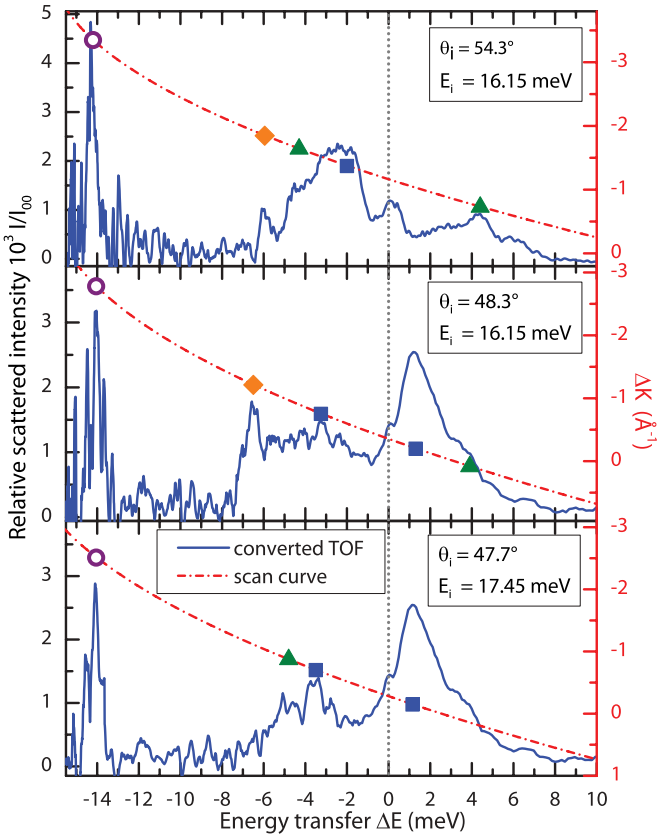

FIG. 3. (Color online) Same as Fig. 2 for the $\overline{\Gamma M}$ direction and with the crystal at $T_S = 103$ K.

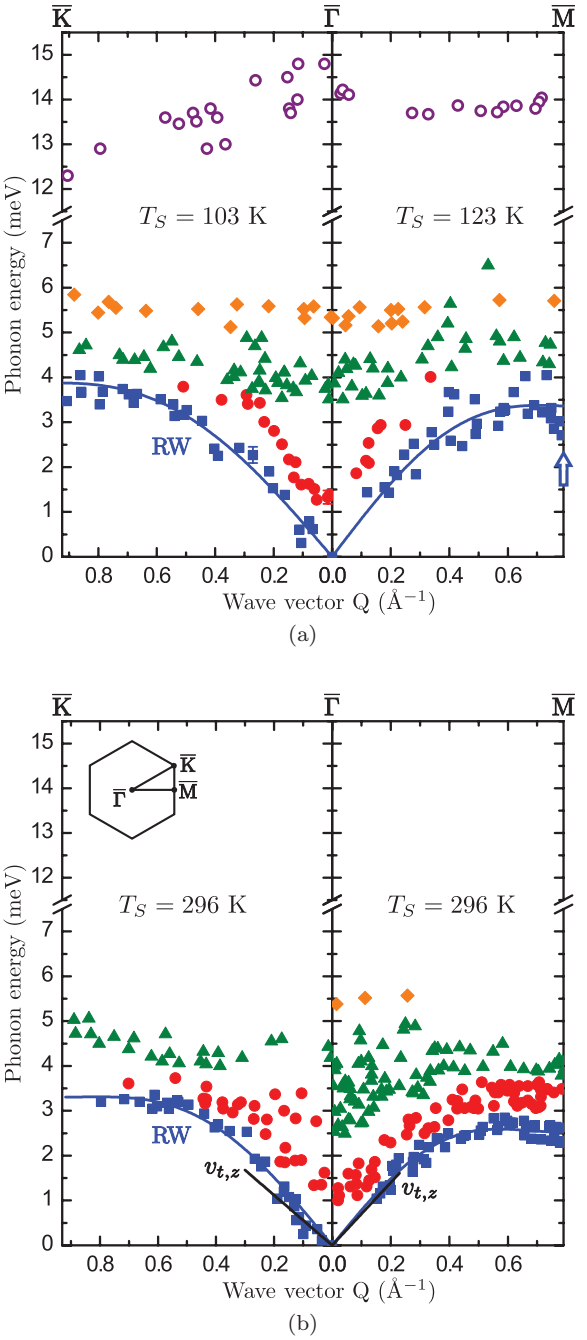

FIG. 4. (Color online) Measured surface phonon dispersion relation of Bi(111). The solid blue lines represent a fit of the Rayleigh mode (RW) by a simple force constant model. The black lines show the velocity of the shear transverse sound in bulk bismuth ($v_{t,z}$). The different symbols correspond to the different peaks in the scan curves in Figs. 2 and 3. (a) Sample cooled down to T_S. The blue arrow indicates a possible anomaly at the $\overline{M}$ point. (b) Sample at room temperature.

observed branches is certainly more than one would expect for a monoatomic surface as well as those ordinarily found in low-index metal surfaces.[27] A similar situation was found for Pb(111) multilayers on copper,[28] providing evidence that HAS from surfaces with a strong e-p interaction can also detect phonons localized a few layers beneath the surface.[10] The DFPT analysis presented in the next section confirms that this is the case also for the (111) surface of bismuth.

The lowest surface branch, corresponding to the ordinary Rayleigh wave (RW), is well reproduced [Fig. 4(a), full line] by a simple force constant model for a single atomic layer with nearest and next-nearest neighbor interactions except at the point where something like a sharp anomaly is observed [Fig. 4(a), arrow]. An inspection of the experimental surface electronic band structure (Ref. 29, or Fig. 11(c) of Ref. 1) suggests that this anomaly corresponds to a nesting between the surface hole pocket state at ± 0.2 Å^{-1} and the surface electron pocket state of equal spin at ± 0.6 Å^{-1}.

The comparison of low-temperature data with those collected at RT in the acoustic region, Fig. 4(b), provides a hint towards a surface anharmonicity. Note that phonons in the acoustic region exhibit energies in temperature units below 80 K, so that the count rate at RT is almost three times higher than at 100 K. This apparent advantage is however frustrated by the increase of the multiphonon width and background with T, which dramatically reduces resolution in a system with several low-energy dispersion curves and yields a larger spread of data points. Nevertheless the phonon branches in the acoustic region and the thermal softening of the RW branches are well discernible.

There is substantial overall softening of the whole RW branch with respect to the low-temperature data: The RW velocity at small Q and low T as derived from a simple force-constant model fit of the RW dispersion curve

in Fig. 4(a) is (8.1 ± 0.4) meV Å along $\overline{\Gamma K}$ and (8.3 ± 0.4) meV Å along $\overline{\Gamma M}$. At room temperature the velocities derived from Fig. 4(b) are reduced to (7.3 ± 0.3) meV Å for $\overline{\Gamma K}$ and (7.5 ± 0.3) meV Å along $\overline{\Gamma M}$. Note that these values are substantially larger than the corresponding velocities of the shear vertical (SV) transverse sound in bulk bismuth (at RT: $v_{t,z} = 5.59$ meV Å along $\overline{\Gamma K}$, and 7.38 meV Å along $\overline{\Gamma K}$),[30] the reason being the initial upward curvature of the bulk dispersion curve of SV transverse modes typical of layered structures. However, the thermal softening of the RW velocities at small Q, -8.1% (-0.042%/K) along $\overline{\Gamma K}$ and -9.8% (-0.057%/K) along $\overline{\Gamma M}$, indicates an isotropic anharmonicity in the two surface directions and is appreciably larger than that of the corresponding bulk velocities $v_{t,z}$ (-4.9% and -5.3%, respectively) as interpolated from Eckstein *et al.*[30] A larger anharmonicity at the surface than in the bulk is expected and is usually related to a larger mean-square SV displacement or equivalently to a smaller Debye temperature at the surface.[16]

At the zone boundary, however, the softening of the RW frequency is considerably anisotropic: -10.8% (-0.06%/K) at $\overline{K}$ and -21.9% (-0.11%/K) at $\overline{M}$. The large softening at $\overline{M}$ suggests that the $\overline{M}$-point anomaly is still there, though much broadened by the increase of temperature. Such a large temperature dependence is not expected for a phonon which for kinematic reasons could only decay through a quartic anharmonic process. Thus the anomaly could be of the nonadiabatic type mentioned in the introduction, with a strong e-h character.[15]

IV. THEORY

A. DFPT dispersion curves and comparison with experiment

The dynamical properties of the Bi(111) surface were calculated by means of density functional perturbation theory (DFPT)[31] as implemented in the QUANTUM-ESPRESSO package.[32] A relativistic norm-conserving pseudopotential with five valence electrons and the Perdew-Burke-Ernzerhof approximation[33] for the exchange-correlation energy functional was used.

The electron wave functions were expanded in plane waves up to an energy cutoff of 45 Ry. A Gaussian smearing of 0.01 Ry was introduced in the occupation of states to deal with the metallic character of Bi. We optimized the bulk geometry by integrating over a $12 \times 12 \times 12$ Monkhorst-Pack mesh[34] in the Brillouin zone (BZ). The resulting equilibrium rhombohedral parameters at 0 K obtained by discarding the SOC are $a = 4.786$ Å, $\alpha = 57.03^\circ$, $z = 0.2349$ and $a = 4.816$ Å, $\alpha = 57.42^\circ$, $z = 0.2357$ by including SOC, in comparison with the experimental values of $a = 4.724$ Å, $\alpha = 57.35^\circ$, and $z = 0.237$,[18] where the z parameter indicates the position of the Bi atom on the site $\pm(z,z,z)$ in the Wyckoff notation. The corresponding calculated lattice parameters of the conventional bulk hexagonal unit cell containing three bilayers are $a_{\mathrm{hex}} = 4.569$ Å, $c_{\mathrm{hex}} = 11.979$ Å without SOC, $a_{\mathrm{hex}} = 4.627$ Å and $c_{\mathrm{hex}} = 12.022$ Å with SOC, as compared to the experimental values $a_{\mathrm{hex}} = 4.538$ Å and $c_{\mathrm{hex}} = 11.798$ Å.

The Bi lattice with free (111) surfaces was modeled by a slab including 6 bilayers. The slab-adapted hexagonal unit cell contains one single atom per layer. Periodicity normal to the slab (z direction) is recovered by intercalating periodically repeated slabs with vacuum gaps of 12 Å. The hexagonal surface Brillouin zone (SBZ) was sampled over a $8 \times 8 \times 1$ Monkhorst-Pack grid. The atomic positions were relaxed until forces became smaller than 0.1 mRy/a.u. The dynamical matrix was calculated on an 8×8 mesh of $\mathbf{Q}$ points in the SBZ. A calculation for 6 bilayers with SOC performed at the $\overline{\Gamma}$ point shows a softening of the phonon energies with respect to those calculated without SOC similar to that found for bulk phonons.[18] The softening corresponds to at most 10% for the optical branches and 4% for acoustic branches. DFPT calculations including SOC for slabs of increasing thickness of 1 to 5 bilayers[19] show that such softening affects the whole set of phonon dispersion curves. The effect of SOC on the structural parameters is relatively small although it induces a sensible change in the phonon dispersion relations of bulk Bi.[18] With DFPT calculations including SOC, which are computationally heavy and necessarily restricted to slabs of only a few bilayers, the first bilayer turns out to be slightly compressed, rather than slightly expanded as in the experiment.[16] For the 6-bilayer slab, the contraction of the outermost bilayer turns out to be -0.83%, while the distance between the first and second bilayer is expanded by 3.13%. It should be noted that the phonon stiffening possibly arising from the contraction of the first bilayer may to some extent compensate the SOC softening, which may explain why DFPT calculations without SOC on thin slabs reproduce fairly well the experimental dispersion curves, as shown in the next section. In any case, they prove to be sufficiently accurate to determine the character of the observed phonon branches.

The full set of calculated dispersion relations along the symmetry directions is shown in Fig. 5 together with the corresponding phonon densities projected onto the first, second, and third layer for shear vertical (SV1, SV2, SV3) and longitudinal (L1, L2, L3) polarizations. The color code measuring the phonon densities is shown in the inset on the right. The projected densities of SH modes have been omitted since planar He scattering from SH modes is forbidden by symmetry along the $\overline{\Gamma M}$ direction and is negligibly small along $\overline{\Gamma K}$ due to the approximate mirror symmetry of the surface charge density in this direction [Fig. 1(d)].

The complete set of dispersion curves, also including shear-horizontal (SH) modes, is shown in Fig. 6 for a 20-bilayer slab. The calculation is performed with the usual filling procedure, by which a bulk slab of 14 bilayers with its calculated bulk force constant is sandwiched between the two halves of the present 6-bilayer slab with its actual force constants. The labels indicate the surface branches of sagittal polarization (either SV or L) appearing in Fig. 5, which are distinctly localized outside the surface-projected bulk bands.

Notable features of the calculated dispersion curves similar to those already predicted for Sb(111)[9] are

(i) a localized SV1 + SV2 branch (15.3 meV at $\overline{\Gamma}$) above and a strong SV3 edge resonance at the maximum of the bulk optical band;

(ii) an L1 + L2 resonance in the acoustic region which is starting from 1.2 meV at $\overline{\Gamma}$ rather than from zero as for the usual longitudinal resonance in metal surfaces;[27]

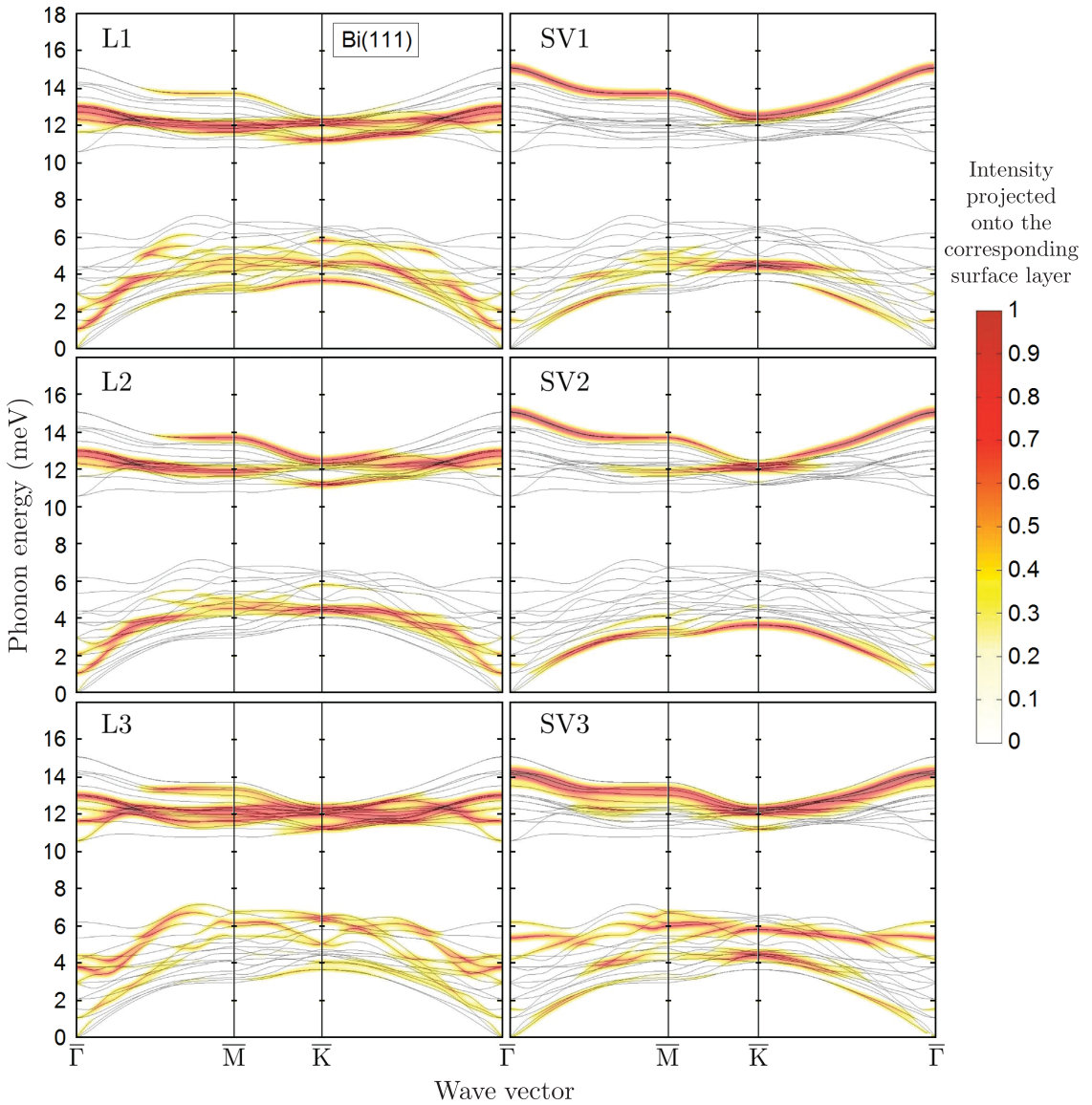

FIG. 5. (Color online) Dispersion curves of a Bi(111) 12-layer slab from a DFPT calculation without SO coupling. Highlighted branches represent surface-localized modes and resonances for longitudinal (L) (left panel) and shear vertical (SV) (right panel) polarization. Their intensity projected respectively onto the first, second, and third surface layer is given by the gray code.

(iii) moderately intense L3 and SV3 resonant branches starting at $\overline{\Gamma}$ from 3.8 meV and 5.4 meV, respectively, and a strong flat L3 resonant branch in the optical region.

The set of longitudinal branches L1, L2, and L3 shows large avoided crossings in both symmetry directions similar to those found in normal fcc metals such as Cu(111) and Al(111).[27] All of these features are in some way related to a stiffening of the inner force constants in the two top bilayers due to the presence of occupied surface states. No surface mode is predicted in the acousto-optical gap. At long wavelengths the RW branch runs near the edge of the bulk transverse acoustic band with a dominant SV1 + SV2 polarization and a negligible L1 + L2 component, but near the $\overline{\text{K}}$ point (and to a minor extent at $\overline{\text{M}}$) the surface component of the RW acquires a longitudinal polarization, the SV1 intensity being transferred to an upper strong resonance at 4.4 meV.

A comparison of the experimental data with the most prominent calculated surface phonon branches is plotted in Fig. 7. Therefore the dispersion curves of Fig. 5 which contribute the largest DOS are superimposed on the experimental data with an indication of the respective polarizations. The broad features of the projected density (Fig. 5) were reduced to a single line whose energy $\hbar\omega$ corresponds to a weighted average $\omega(q) = \sum_i \omega_i p_i / \sum_i p_i$ where p_i are the projections. While for most polarizations the width of the projected density is smaller than the uncertainty of the experimental data, the L1 mode is the only one considerably affected by this procedure. It should also be noted that L1 is hybridized with SV1 with a transfer of intensity towards $\overline{\text{K}}$.

Figure 7 shows an overall good agreement and allows a full assignment of the experimental branches to well-defined phonon modes. In practice all expected branches of sagittal polarization are observed. The most surprising fact

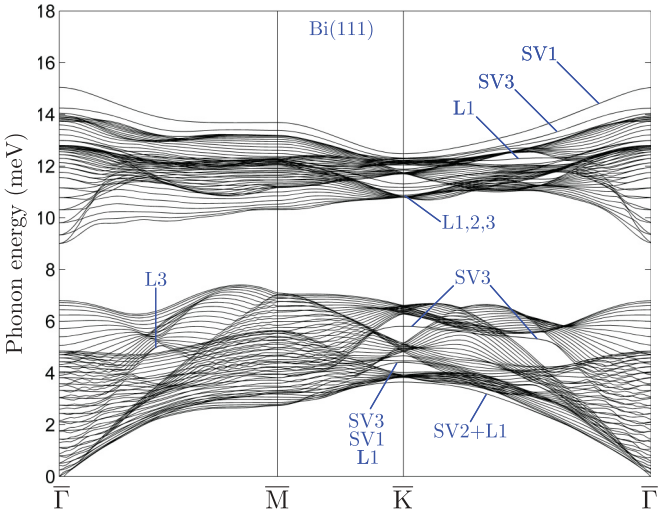

FIG. 6. (Color online) DFPT phonon dispersion curves of a 20-bilayer slab of Bi(111) obtained with the filling procedure by which a bulk slab of 14 bilayers with its DFPT bulk force constant is sandwiched between the two halves of the present 6-bilayer slab with its actual force constants. The labels indicate the surface branches of sagittal polarization which are distinctly localized outside the surface-projected bulk bands (notations as in Fig. 5).

is the observation of the L3 and SV3 branches since their displacement field is mostly localized in the second bilayer. The latter is even visible in both the acoustic and optical regions. The observation of these subsurface phonons by HAS is supposed to be caused by the same electron-phonon mechanism that has been observed for ultrathin Pb(111) films[10] and will be explained in the following.

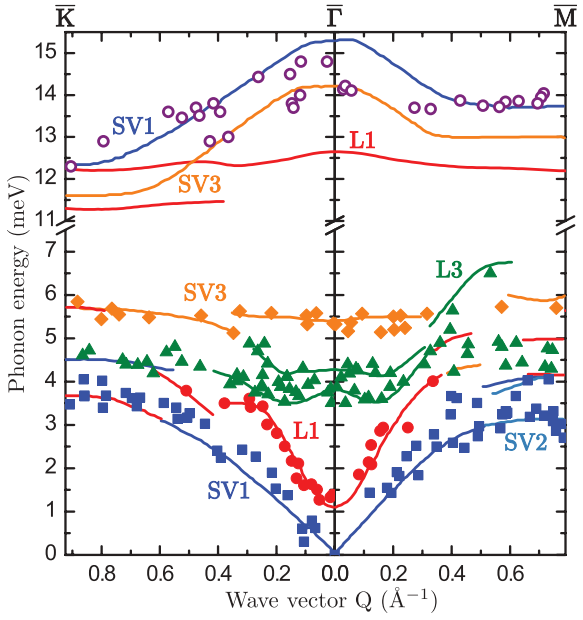

FIG. 7. (Color online) Comparison of the measured phonon dispersion relation with the DFPT calculations. The calculated surface phonon branches of Fig. 5 which contribute the largest DOS are superimposed onto the experimental data points.

B. Phonon-induced charge-density oscillations

By assuming that the scattering potential of the He atom is proportional to the charge density via the Esbjerg-Nørskov constant[35] A, the inelastic (one-phonon) transition probability of the He atom from the initial state of wave vector $\mathbf{k}_i$ to the final state of wave vector $\mathbf{k}_f$ is given, up to a constant, by[10]

$$P(\mathbf{k}_i,\mathbf{k}_f) \propto \frac{k_f}{|k_{iz}|}[1+n_{BE}(\Delta E)]A^2 \sum_{\mathbf{Q}\nu} |\langle \mathbf{k}_f|\delta n(\mathbf{Q}\nu,\mathbf{r})|\mathbf{k}_i\rangle|^2 \times \delta(\Delta E - \varepsilon_{\mathbf{Q}\nu}) \propto f(\Delta E)N(E_F)\sum_{\mathbf{Q}\nu}\lambda_{\mathbf{Q}\nu}\delta(\Delta E-\varepsilon_{\mathbf{Q}\nu}), \quad (2)$$

where $\delta n(\mathbf{Q}\nu,\mathbf{r})$ is the charge-density oscillation (CDO) produced at position $\mathbf{r}$ by a surface phonon of parallel wave vector $\mathbf{Q}$ and branch index ν, and $n_{BE}(\Delta E)$ is the Bose-Einstein occupation number for the phonon of energy $\Delta E = \varepsilon_{\mathbf{Q}\nu}$. The Fourier transform of time-dependent quantities is implicit in Eq. (1), resulting in energy-conservation δ functions. As shown in Ref. 10, each individual surface-phonon contribution to $P(\mathbf{k}_i,\mathbf{k}_f)$ in Eq. (1) turns out to be weighed by the respective e-p interaction strength $\lambda_{\mathbf{Q}\nu}$ (the *mode* λ) and by a weakly energy-dependent prefactor $f(\Delta E)N(E_F)$, where $N(E_F)$ is the electronic density of states at the Fermi level.

The CDOs $\delta n(\mathbf{Q}\nu,\mathbf{r})$ have been calculated with DFPT at the $\overline{\Gamma}$ point ($\mathbf{Q}=0$), for the surface optical modes SV1 (15.3 meV) and SV3 (14.2 meV) and for the acoustic-band resonances L1 (1.2 meV), L3 (3.8 meV), and SV3 (5.4 meV). The calculation is made for frozen-phonon displacements equal to the quantum $(\hbar^2/2M\varepsilon_{0\nu})^{1/2}\mathbf{e}_{0\nu}(l)$, where M is the Bi atom mass and $\mathbf{e}_{0\nu}(l)$ the normalized phonon eigenvector at the lth layer. The contour lines of the resulting CDOs with respect to the static charge density are plotted in Fig. 8 for values of $\pm 2^{-n}\times 10^{-4}$ a.u. with $n=0,1,2,\ldots,7$ and signs + (red lines) or − (blue lines) corresponding to a charge-density increase or decrease, respectively.

As seen in Fig. 1(d), the HAS classical turning point is somewhere between 2.6 and 3.4 Å depending on where the He atom hits the surface, say at an average distance of 3 Å. At this distance the mode SV1 (15.3 meV) at $\overline{\Gamma}$ produces an average oscillation of $(1/32)\times 10^{-4}$ a.u., which is about a factor of 2 larger than that of the SV3 mode at 5.4 meV and a factor of 4 larger than L1 at 1.2 meV. The oscillations of SV3 (14.2 meV) and L3 (4.4 and 3.8 meV) are even smaller. However, when these contributions to the transition probability are corrected by the respective Bose-Einstein factors at 123 K, the predicted scattering intensities fulfill the hierarchy observed in the experiment. This can be appreciated in Fig. 8(a), where the wave vectors of L1, L3 (4.4 meV and 3.8 meV), SV3, and the optical SV1 modes associated with the experimental peaks $Q = 0.15$, 0.06, −0.05, −0.16, and $-G-0.23$ Å^{-1} ($G = 1.6$ Å^{-1} = reciprocal lattice vector), respectively, are all fairly close to $\overline{\Gamma}$. Note that the optical mode SV1 is observed through an umklapp process: Such process would not be possible in flat ordinary metal surfaces but it acquires a large intensity on Bi(111) due to the surface corrugation which lends the necessary G vector.

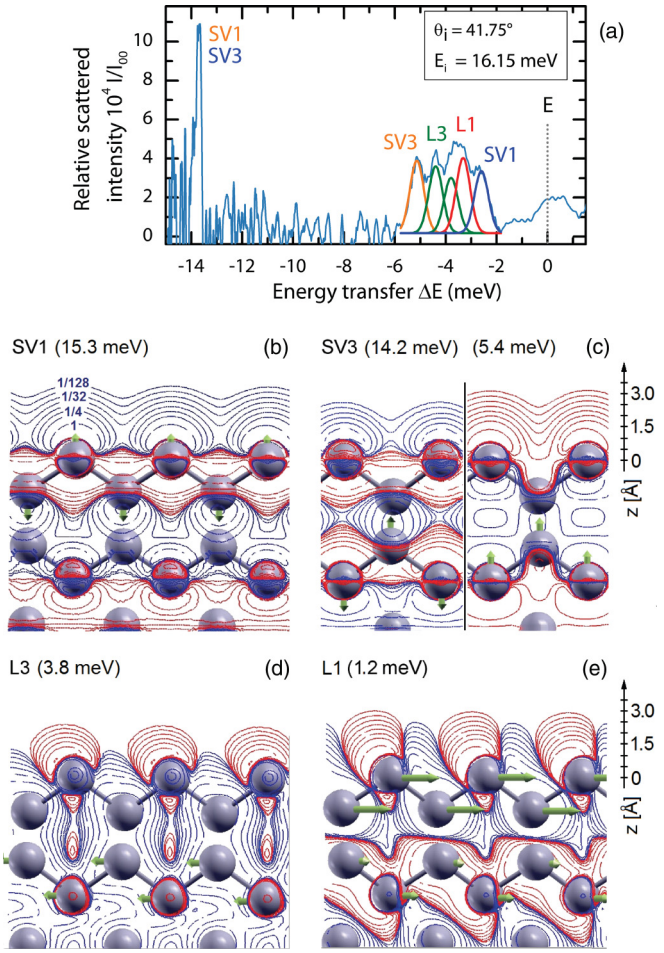

FIG. 8. (Color online) (a) Energy transfer spectrum for helium atoms scattered from Bi(111) along $\overline{\Gamma M}$ with the crystal cooled down to $T_S = 123$ K. The spectrum was least-squares fitted by multiple Gaussian peaks. Note that the optical SV1 peak is narrower than those of the acoustic band because the latter are all resonances whereas the optical mode SV1 is localized at the surface. (b)–(d) CDOs calculated with DFPT at the $\overline{\Gamma}$ point induced by frozen phonon displacements. The contour lines of the resulting CDOs with respect to the static charge density show the corresponding increase (red lines) or decrease (blue lines), respectively.

The calculation of the CDOs confirms that the phonons observed in the upper part of the acoustic band are associated with third-layer (second-bilayer) SV3 and L3 resonances. In particular the SV3 mode has an intensity comparable to the first-layer modes L1 and SV1. On the contrary, the optical SV3 mode has a CDO which is about eight times smaller than that of the optical SV1 with about the same Bose-Einstein factor. Thus, although the peak energy and wave vector are closer to the predicted SV3 than to the SV1 branch, the peak at 13.8 meV has to be assigned to SV1. SOC calculations yield softer optical surface modes in better agreement with the experiment. Note that the width of the optical SV1 peak in Fig. 8(a) is narrower than that of the peaks composing the acoustic band structure since the former is a localized surface branch whereas the latter are all resonances in the acoustic continuum.

The sharp anomaly observed at the $\overline{M}$ point is not reproduced by the DFPT calculation, similar to what was experienced with the sharp anomaly of H(1 × 1):W(110).[15,36] This supports the conjecture of a nonadiabatic nature of this anomaly and its electron-hole excitation character, as argued in the previous section.

C. Estimating the Bi(111) electron-phonon interaction

The integrated one-phonon transition probability $I_{1\mathrm{ph}} = \int P(\mathbf{k}_i,\mathbf{k}_f)dE$, when divided by the corresponding total elastic intensity I_{el} for the given incident energy and angle, gives under the approximation of a constant $f(\Delta E) \equiv \bar{f}$

$$I_{1\mathrm{ph}}/I_{el} \propto \bar{f}N(E_F)\sum_{\mathbf{Q}\nu}\lambda_{\mathbf{Q}\nu} \propto \bar{f}N(E_F)\lambda. \quad (3)$$

This equation would allow for an estimation of the e-p mass-enhancement parameter λ for a conducting surface from the integrated relative one-phonon HAS intensity once the proportionality constant is known. On the other hand, Eq. (2) may be used to estimate λ for Bi(111) by comparing its one-phonon HAS intensities to those measured on similar surfaces under similar kinematic conditions, e.g., those on Pb(111) multilayers.[10,37]

As a simple example, let us restrict ourselves to the integration on the creation side of the energy scale of the TOF spectrum relative to the total elastic (specular plus diffraction) intensity at a given incident energy and angle: For example, for $E_i = 16.15$ meV and $\theta_i = 41.75°$ Fig. 8(a) yields $I_{1\mathrm{ph}}/I_{el} = 5.7 \times 10^{-4}$. Similarly for a 7 monolayer (ML) sample of Pb(111)/Cu, for which λ[7 ML Pb(111)] = 0.96, the relative integrated TOF spectrum at 42° and $E_i = 22$ meV along $\overline{\Gamma M}$[10,37] is $I_{1\mathrm{ph}}/I_{el} = 7.5 \times 10^{-4}$.

Assuming the same $\bar{f}$ for Bi(111) and 7 ML Pb(111) due to the nearly equal kinematic conditions of the two HAS experiments and using for the calculated electronic DOS at the Fermi level projected onto the first layer the calculated values $N(E_F) = 0.385$ eV for Bi(111) and 0.682 eV for Pb(111), one can estimate from Eq. (2) λ[Bi(111)]/λ[7 ML Pb(111)] ≈ 1.35 and λ[Bi(111)] ≈ 1.3. This value falls in the wide range discussed by Hofmann, though it should be considered as a rough estimation based on rather qualitative arguments. A more comprehensive integration of the inelastic HAS spectra should, however, provide a more reliable estimation of the e-p coupling strength at the surface of metals and semimetals.

V. SUMMARY

A thorough investigation of the surface phonon dispersion curves of Bi(111) by means of inelastic helium atom scattering has revealed a rich set of dispersion curves in both the acoustic and optical regions. Besides the usual Rayleigh waves, a localized branch above the optical bulk phonon band has been measured in both symmetry directions. In order to assign the observed phonon branches, calculations of the phonon dispersion curves based on density functional perturbation theory have been performed for a six-bilayer self-standing Bi(111) slab. Although the inclusion of the spin-orbit coupling

is recognized to produce some softening of the upper phonon branches, the calculations without SOC proved to be in satisfactory agreement with experiment and to provide a reliable assignment of the phonon branches to well-defined phonon types and polarizations.

The phonon branches running in the upper part of the acoustic region have been associated with shear-vertical and longitudinal phonons localized on the third surface layer (second bilayer). The surprising HAS ability to detect subsurface phonons is analogous to what was previously observed for ultrathin Pb(111) films in the range of 3 to 8 monolayers[28] and has been similarly attributed to the comparatively strong e-p interaction.[10] A DFPT calculation of the phonon-induced surface charge-density oscillations qualitatively confirms this interpretation.

The e-p interaction expressed by the mass-enhancement parameter λ exhibits an increase at the Bi(111) surface in comparison to the small value attributed to the bulk. This increased e-p interaction is consistent with the surface superconductivity reported for polycrystalline Bi and oriented Bi interfaces and the undetectable superconductivity of bulk bismuth. In order to demonstrate the potential of HAS to provide information about the surface e-p interaction, the mass-enhancement parameter for the Bi(111) surface is estimated from a direct comparison of the integrated HAS intensity for a given TOF spectrum in Bi(111) with that measured in a 7 ML Pb(111) sample under similar kinematic conditions. The value estimated in this way, $\lambda \approx 1.3$, is close to that of ultrathin Pb films and is consistent with the reported superconducting critical temperatures of polycrystalline Bi.[3,4]

Finally, an anomaly at the $\overline{\mathrm{M}}$ point, quite sharp at 123 K but very broad at room temperature, is attributed to recombination processes of bulk $\overline{\mathrm{M}}$-point pocket electrons with bulk pocket holes at either $\overline{\Gamma}$ or equivalent $\overline{\mathrm{M}}$ points. The fact that the inelastic HAS probability is proportional to the surface electron density correlation function[10] implies not only that surface and subsurface phonons in a conducting surface are excited via the e-p interaction but also that HAS can excite (or recombine) electron-hole (e-h) pairs or even low-energy collective excitations such as acoustic surface plasmons (ASPs). While many inelastic peaks observed in the present TOF spectra are likely to be related to interpocket e-h recombination processes, some indication that ASP excitations in copper and gold low-index surfaces can be observed with high-resolution spin-echo ^{3}He scattering spectroscopy[38] has been recently reported.[39]

Finally it should be noted that single-particle excitations of conduction electrons by HAS also occur in ordinary metal surfaces, but the extended character of the Fermi surface yields a rather diffuse scattering background, undistinguishable from the anharmonic one. On the contrary, in semimetals the localization of electron and hole pockets in restricted regions of the Q space at the Fermi level gives rise to quasielastic interpocket transitions around fairly well defined values of Q which can be observed with HAS. Thus the study of semimetal surfaces including those of various topological insulators represents a new wide territory of investigation for inelastic helium atom scattering in both its traditional setting[22,26,40] and for the novel spin-echo ^{3}He scattering spectrometers with their unprecedented 20 neV resolution.[38]

ACKNOWLEDGMENTS

This research was supported by the European Commission and the Styrian Government within the ERDF program. One of us (G.B.) acknowledges the Alexander-von-Humboldt Stiftung for support and many useful discussions with E. V. Chulkov, P. M. Echenique, and V. Chis (DIPC, Donostia/San Sebastian, Spain) and J. P. Toennies (Max-Planck-Institut für Dynamik und Selbstorganisation, Göttingen, Germany).

*tamtoegl@tugraz.at

[1] P. Hofmann, Prog. Surf. Sci. **81**, 191 (2006).
[2] J. E. Gayone, S. V. Hoffmann, Z. Li, and P. Hofmann, Phys. Rev. Lett. **91**, 127601 (2003).
[3] B. Weitzel and H. Micklitz, Phys. Rev. Lett. **66**, 385 (1991).
[4] F. Muntyanu, A. Gilewski, K. Nenkov, A. Zaleski, and V. Chistol, Solid State Commun. **147**, 183 (2008).
[5] C. R. Ast and H. Höchst, Phys. Rev. Lett. **87**, 177602 (2001).
[6] J. Gayone, C. Kirkegaard, J. Wells, S. Hoffmann, Z. Li, and P. Hofmann, Appl. Phys. A **80**, 943 (2005).
[7] P. Hofmann, I. Y. Sklyadneva, E. D. L. Rienks, and E. V. Chulkov, New J. Phys. **11**, 125005 (2009).
[8] K. Sugawara, T. Sato, S. Souma, T. Takahashi, M. Arai, and T. Sasaki, Phys. Rev. Lett. **96**, 046411 (2006).
[9] D. Campi, M. Bernasconi, and G. Benedek, Phys. Rev. B **86**, 075446 (2012).
[10] I. Y. Sklyadneva, G. Benedek, E. V. Chulkov, P. M. Echenique, R. Heid, K.-P. Bohnen, and J. P. Toennies, Phys. Rev. Lett. **107**, 095502 (2011).
[11] G. Brusdeylins, R. Rechsteiner, J. G. Skofronick, J. P. Toennies, G. Benedek, and L. Miglio, Phys. Rev. Lett. **54**, 466 (1985).
[12] G. Bracco, R. Tatarek, S. Terreni, and F. Tommasini, Phys. Rev. B **34**, 9045 (1986).
[13] X. Zhu, L. Santos, R. Sankar, S. Chikara, C. Howard, F. C. Chou, C. Chamon, and M. El-Batanouny, Phys. Rev. Lett. **107**, 186102 (2011).
[14] X. Zhu, L. Santos, C. Howard, R. Sankar, F. C. Chou, C. Chamon, and M. El-Batanouny, Phys. Rev. Lett. **108**, 185501 (2012).
[15] E. Hulpke and J. Lüdecke, Phys. Rev. Lett. **68**, 2846 (1992).
[16] H. Mönig, J. Sun, Y. M. Koroteev, G. Bihlmayer, J. Wells, E. V. Chulkov, K. Pohl, and P. Hofmann, Phys. Rev. B **72**, 085410 (2005).
[17] J. Yarnell, J. Warren, R. Wenzel, and S. Koenig, IBM J. Res. Dev. **8**, 234 (1964).
[18] L. E. Díaz-Sánchez, A. H. Romero, and X. Gonze, Phys. Rev. B **76**, 104302 (2007).
[19] V. Chis, E. V. Chulkov, and G. Benedek (unpublished).
[20] M. Mayrhofer-Reinhartshuber, A. Tamtögl, P. Kraus, K. H. Rieder, and W. E. Ernst, J. Phys.: Condens. Matter **24**, 104008 (2012).
[21] A. Tamtögl, M. Mayrhofer-Reinhartshuber, N. Balak, W. E. Ernst, and K. H. Rieder, J. Phys.: Condens. Matter **22**, 304019 (2010).

[22]R. B. Doak, in *Atomic and Molecular Beam Methods*, edited by G. Scoles (Oxford University Press, New York, 1992), Vol. 2, pp. 384–443.
[23]L. Bewig, U. Buck, S. R. Gandhi, and M. Winter, Rev. Sci. Instrum. **67**, 417 (1996).
[24]L. K. Verheij and P. Zeppenfeld, Rev. Sci. Instrum. **58**, 2138 (1987).
[25]G. Benedek, Phys. Rev. Lett. **35**, 234 (1975).
[26]S. A. Safron, Adv. Chem. Phys. **95**, 129 (1996).
[27]G. Benedek, M. Bernasconi, V. Chis, E. Chulkov, P. M. Echenique, B. Hellsing, and J. P. Toennies, J. Phys.: Condens. Matter **22**, 084020 (2010).
[28]J. Braun, P. Ruggerone, G. Zhang, J. P. Toennies, and G. Benedek, Phys. Rev. B **79**, 205423 (2009).
[29]M. Hengsberger, P. Segovia, M. Garnier, D. Purdie, and Y. Baer, Eur. Phys. J. B **17**, 603 (2000).
[30]Y. Eckstein, A. W. Lawson, and D. H. Reneker, J. Appl. Phys. **31**, 1534 (1960).
[31]S. Baroni, S. de Gironcoli, A. Dal Corso, and P. Giannozzi, Rev. Mod. Phys. **73**, 515 (2001).
[32]P. Giannozzi, S. Baroni, N. Bonini, M. Calandra, R. Car, C. Cavazzoni, D. Ceresoli, G. L. Chiarotti, M. Cococcioni, I. Dabo *et al.*, J. Phys.: Condens. Matter **21**, 395502 (2009).
[33]J. P. Perdew, K. Burke, and M. Ernzerhof, Phys. Rev. Lett. **77**, 3865 (1996).
[34]H. J. Monkhorst and J. D. Pack, Phys. Rev. B **13**, 5188 (1976).
[35]N. Esbjerg and J. K. Nørskov, Phys. Rev. Lett. **45**, 807 (1980).
[36]C. Bungaro, S. de Gironcoli, and S. Baroni, Phys. Rev. Lett. **77**, 2491 (1996).
[37]G. Zhang, Ph.D. thesis, University of Göttingen, 1990.
[38]A. P. Jardine, S. Dworski, P. Fouquet, G. Alexandrowicz, D. J. Riley, G. Y. H. Lee, J. Ellis, and W. Allison, Science **304**, 1790 (2004).
[39]P. R. Cole and G. Benedek, Int. Conf. on Solid Films and Surfaces, Genoa 1-6 July 2012, (abstract PLA1.2) http://icsfs16.fisica.unige.it/?page=Contents&tab=Abstracts.
[40]G. Benedek and J. Toennies, Surf. Sci. **299-300**, 587 (1994).